# Structure and Dynamics of CO$_2$ on Rutile TiO$_2$(110)-1×1

Xiao Lin,[†,‡] Yeohoon Yoon,[†,‡] Nikolay G. Petrik,*[†] Zhenjun Li,[†] Zhi-Tao Wang,[§] Vassiliki-Alexandra Glezakou,[†] Bruce D. Kay,[†] Igor Lyubinetsky,[§] Greg A. Kimmel,[†] Roger Rousseau,*[†] and Zdenek Dohnálek*[†]

[†]Fundamental and Computational Sciences Directorate, [§]Environmental Molecular Sciences Laboratory, Pacific Northwest National Laboratory, P.O. Box 999, Richland, Washington 99352, United States

Ⓢ Supporting Information

ABSTRACT: Adsorption, binding, and diffusion of CO$_2$ molecules on model rutile TiO$_2$(110)-1×1 surfaces were investigated experimentally using scanning tunneling microscopy, infrared reflection adsorption spectroscopy (IRAS), molecular beam scattering, and temperature programmed desorption and theoretically via dispersion corrected density functional theory and ab initio molecular dynamics. In accord with previous studies, bridging oxygen (O$_b$) vacancies (V$_O$'s) are found to be the most stable binding sites. Additional CO$_2$ adsorbs on 5-coordinated Ti sites (Ti$_{5c}$) with the initial small fraction stabilized by CO$_2$ adsorbed on V$_O$ sites. The Ti$_{5c}$-bound CO$_2$ is found to be highly mobile at 50 K at coverages of up to 1/2 monolayer (ML). Theoretical studies show that the CO$_2$ diffusion on Ti$_{5c}$ rows proceeds via a rotation-tumbling mechanism with extremely low barrier of 0.06 eV. The Ti$_{5c}$-bound CO$_2$ molecules are found to bind preferentially to a single Ti$_{5c}$ with the O=C=O axis tilted away from the surface normal. The binding energy of tilted CO$_2$ molecules changes only slightly with changes in the azimuth of the CO$_2$ tilt angle. At 2/3 ML, CO$_2$ diffusion is hindered and at 1 ML an ordered (2×2) overlayer with a zigzag arrangement of tilted CO$_2$ molecules develops along the Ti$_{5c}$ rows. Out of phase arrangement of the zigzag chains is observed across the rows. An additional 0.5 ML of CO$_2$ can be adsorbed at O$_b$ sites with a binding energy only slightly lower than that on Ti$_{5c}$ sites presumably due to quadrupole−quadrupole interactions with the Ti$_{5c}$-bound CO$_2$ molecules.
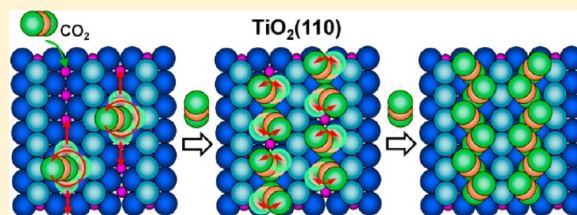
1. INTRODUCTION

As the environmental impact of CO$_2$ emissions mounts, the need for technologically advanced solutions for CO$_2$ capture, conversion, or sequestration increases. To facilitate such solutions, a deeper fundamental understanding of CO$_2$ activation is required to develop more efficient routes for CO$_2$ conversion to fuels and to refine our understanding of impacts caused by CO$_2$ sequestration.[1−4] Due to its benign nature and low energy content, CO$_2$ attracted very little attention in the past and much less is known about its interactions with well-defined surfaces in comparison to other simple molecules such as H$_2$, CO, and H$_2$O. This is evidenced by the fact that only one surface science review article has focused on the fundamentals of CO$_2$ interactions with single crystalline surfaces.[5] This is further amplified on oxide surfaces, an area of our interest, that remain largely unexplored. Recent interest in understanding CO$_2$ interactions with oxides is documented by a number of reports on model oxide surfaces such as Zn-terminated ZnO(0001),[6] ZnO(10$\bar{1}$0),[7] CaO/Si(100),[8] CaO(100),[9] TiO$_2$(110),[10,11] MgO(100),[12] Cr$_2$O$_3$(0001),[13] Cr$_2$O$_3$(111),[14] RuO$_2$(110),[15,16] and PdO(101).[17]

The interactions of CO$_2$ with TiO$_2$ have been also studied previously.[10,11,18−41] The primary motivation for these studies stems from reports indicating that TiO$_2$ can be used for photoreduction of CO$_2$ to hydrocarbons or methanol.[23,42−45] Additionally, CO$_2$ has also been used as a probe molecule for

characterizing different surface sites on TiO$_2$ surfaces.[11,19,26,27] Most studies have focused on rutile TiO$_2$(110)-(1×1),[10,20,22,24,28,33−35,41] which is the most stable TiO$_2$ surface. Using a combination of temperature programmed desorption (TPD) and high resolution electron energy loss spectroscopy (HREELS) Henderson showed that CO$_2$ initially adsorbs on oxygen vacancies (V$_O$'s) on the bridging oxygen (O$_b$) rows and subsequently on 5-coordinated Ti^{4+} sites (Ti$_{5c}$).[10] On both sites, CO$_2$ binds only weakly and desorbs at ~166 and 137 K, respectively. Later Thompson et al. explored CO$_2$ adsorption on TiO$_2$(110) as a function of reduction and sample annealing temperature.[11] In both studies, the CO$_2$ adsorption measurements were limited by a liquid nitrogen cooling to the base temperature of 110−130 K. Additionally, sticking coefficient measurements as a function of incident energy were reported by Funk and Burghaus.[28] Recent scanning tunneling microscopy (STM) investigations[24,25,34,35,41] have focused on CO$_2$ adsorption on V$_O$ sites at low coverages of CO$_2$ finding that CO$_2$ can be easily reduced to CO by electrons injected from the STM tip with energies above ~1.8 V.[25,34,41] Additionally, the barrier for CO$_2$ diffusion from V$_O$ sites has been determined to be 0.14 eV.[24] Theoretical studies have been limited to static structural models

and determination of the binding energy dependence of CO_2 as a function of coverage with the main emphasis on assigning binding sites and investigating the conversion of CO_2 at the V_O defect sites to CO.[25,34,35] Most recently, a combined STM and dispersion-corrected density functional theory (DFT) study has shown that at low coverage CO_2 on rutile $TiO_2(110)$ is mobile with relatively low diffusion barriers.[24]

In this report, we focus on a detailed understanding of the coverage-dependent binding configurations of CO_2 and their dynamic interconversion. Using low temperature STM, infrared reflection−absorption spectroscopy (IRAS), and TPD in conjunction with DFT calculations and ab initio molecular dynamics (AIMD) simulations we show that V_O's are the most stable binding sites. Additional CO_2 adsorbs on 5-coordinated Ti sites (Ti_{5c}) with the initial small fraction being stabilized by CO_2 adsorbed on V_O's. The Ti_{5c}-bound CO_2 molecules are found to bind to a single Ti_{5c} with the O=C=O axis tilted away from the surface normal at all coverages. The theoretical studies show that diffusion observed at low coverages proceeds via a rotation-tumbling mechanism with the barrier of 0.06 eV. At saturation coverage of 1 monolayer (ML) an ordered (2×2) overlayer with a zigzag arrangement of tilted CO_2 molecules along the Ti_{5c} rows and out-of-phase arrangement across the rows is observed. An additional 0.5 ML of CO_2 can be adsorbed on O_b sites with a binding energy only slightly lower than that on Ti_{5c} sites due to quadrupole−quadrupole interactions with the Ti_{5c}-bound CO_2 molecules.

2. METHODS

2.1. Experimental Details. The experiments were performed in three separate ultrahigh vacuum (UHV) systems: (1) a scanning tunneling microscopy system for spatially resolved imaging,[46] (2) an IRAS/TPD system,[47] and (3) a molecular beam system for absolute CO_2 coverage measurement and TPD studies.[48] The systems are briefly described below.

a. STM System. The STM experiments were carried out in an ultrahigh vacuum chamber (base pressure $\leq 3 \times 10^{-11}$ mbar) equipped with an Omicron variable temperature STM. Well-ordered partially reduced rutile $TiO_2(110)$-(1×1) surfaces were prepared by repeated cycles of Ne^+ sputtering and 950 K annealing of the single crystalline TiO_2 sample (10 × 2 × 0.5 mm^3, Princeton Scientific). The surface order and cleanliness were checked using low energy electron diffraction (LEED) and Auger electron spectroscopy (AES). Electrochemically etched and UHV-annealed tungsten tips were used for imaging. In all experiments, constant current tunneling mode with a positive sample bias voltage was employed. The STM scan rate of ~0.7 ms/point (~2 min/frame) was used and the STM images were analyzed using WSxM software (Nanotech).[49] The concentration of V_O's on the samples ranged from 0.07 to 0.09 monolayer (ML). Carbon dioxide (Matheson, purity 99.995%) was dosed onto the $TiO_2(110)$ at 50 K directly in the STM stage using a retractable tube doser with a 2-μm pinhole aperture.[46]

b. IRAS System. The IRAS and TPD experiments were conducted in a UHV system that has been described previously.[47] Typical base pressures were ~8 × 10^{-11} Torr. The system was equipped with a closed-cycle helium cryostat (Advanced Research Systems CSW 204B), a quadrupole mass spectrometer (Extrel), a molecular beamline for dosing adsorbates, and a Fourier transform infrared spectrometer (Bruker Vertex 70). The infrared light was incident on the $TiO_2(110)$ single crystals at grazing incidence (~84° with respect to normal) and detected in the specular direction.

Two different crystals were used for the measurements of the IRAS spectra with the IR plane of incidence perpendicular to and parallel to the O_b rows (i.e., along the $[1\bar{1}0]$ and $[001]$ azimuths, respectively). The 10 × 10 × 1 mm $TiO_2(110)$ crystals (CrysTec GmbH) were mounted on a resistively heated tantalum base plate. The crystals were prepared by sputtering with 2 keV Ne^+ ions and then annealed for between 2 and 10 min in vacuum at 950 K. The V_O concentration was typically 0.04−0.08 ML, as determined from the high temperature OH recombination peak during water TPD.[50,51] For temperature monitoring and control, a K-type thermocouple was spot-welded to the base plate. During CO_2 TPD, the peak positions can vary within ~10% between different samples and over time for the same sample. This uncertainty arises because the thermal contact between the sample and the base plate varies somewhat from sample to sample and changes as any sample is repeatedly heated and cooled. Despite this uncertainty, the CO_2 TPD spectra reported here agree well with early investigations.[10,11,28]

Most of the IRAS spectra were obtained using a spectrometer resolution, $\Delta \nu$, setting of 4 cm^{-1}. Absorbances are defined as $A(\nu) \equiv \log_{10}[R_0(\nu)/R(\nu)]$, where $R(\nu)$ and $R_0(\nu)$ are the reflected signal from the $TiO_2(110)$ with and without adsorbed molecules. The reported spectra are averages of multiple individual experiments. For each individual experiment, the spectra are the average of 4000 scans of the spectrometer.

c. Molecular Beam (MB) System. This instrument is equipped with AES, LEED, X-ray photoelectron spectroscopy (XPS), a quartz crystal microbalance (QCM, XTM/2-Inficon), and a quadrupole mass spectrometer (QMS, UTI-100C) for TPD studies.

The rutile TiO_2 crystal (10 × 10 × 1 mm^3, Princeton Scientific) with the (110) surface exposed was bonded with ceramic glue (Aremco Ultra-Temp 516) onto a Ta plate as described previously.[48] The temperature (70−900 K) was measured using a thermocouple glued to the edge of the crystal. The TPD spectra (90−800 K, 1.5 K/s) were taken with the crystal in line-of-sight geometry using a UTI quadrupole mass spectrometer. The initial surface cleaning procedure comprised cycles of Ne^+ sputtering (1.5 kV, 10 μA) at 300 K and annealing at 850−900 K for 5−10 min until a clean and ordered $TiO_2(110)$-(1×1) surface was obtained on the basis of AES, XPS, and LEED. To maintain the clean surface, a brief, 3 min sputtering at 300 K followed by 5 min annealing at 850 K was used on a daily bases. Reproducibility of the surface structure was confirmed by H_2O TPD line shape.[10,50] The samples with V_O concentration of ~0.05 ML were used as determined on the basis of the ratio of water recombination desorption peak area at ~500 K to the monolayer desorption peak at 284 K.[10,53]

2.2. Theoretical Methods. All calculations are carried out employing DFT as implemented in the CP2K package[54−56] with gradient-corrected (PBE) functional for exchange and correlation.[57] Core electrons are modeled as norm-conserving pseudopotentials.[58] The wave functions are expanded in a double-ζ Gaussian basis set in which basis superposition errors are minimized[59] with an additional auxiliary plane wave basis of 400 Ry energy cutoff is used for the calculation of the electrostatic energy. Brillouin zone sampling is performed by using Γ-point. The dispersion forces are modeled by the DFT-D method (DFT-D3)[60] where an attractive dispersion coefficient and the corresponding cutoff function are added to the DFT potential to account for long-range interactions. For this approximation, the standard parameter set of Grimme[60] is used with a cutoff of 10 Å.

Our previous work has found that this approach produced adequate potential energy surfaces for hydrocarbons on oxides,[61,62] as well as the structure and spectroscopic properties of liquid super critical CO_2.[63,64] Calculation of all reaction coordinates was performed using the climbing image nudged-elastic-band method (CI-NEB)[65,66] employing 13−17 replicas.

As a surface model, a six TiO_2 trilayer-thick (3×4) rutile TiO_2 (110) slab is adopted with a 10 Å thick vacuum layer to minimize electrostatic interactions between periodic images in the direction of the surface normal. Only the bottom Ti layer is fixed to their bulk lattice positions and all other layers are allowed to relax. For various CO_2 coverages we constructed 1/3, 1/2, 2/3, and 1 monolayer (ML) by placing 4, 6, 8, and 12 CO_2 molecules on the slab, respectively. All simulations are performed by sampling the canonical (NVT) ensemble using molecular dynamics techniques employing Nose−Hoover thermostats[67,68] with a time step of 0.5 fs during more than 20 ps of equilibrated trajectory at the temperature of 130 K.

As a test of the currently used approximations, the binding energy of single CO_2 molecule on the TiO_2 surface is considered for a number of different configurations (Figure S1, Supporting Information). For example, the most stable binding configuration with a binding energy of 0.45 eV is the one with CO_2 perpendicular to the Ti_{5c} row and tilted ~45° with respect to the surface normal along [$1\bar{1}0$] direction in a good agreement with previous studies.[35]

For the model of a reduced TiO_2 surface, one V_O is generated on the same size of the slab so that the V_O coverage becomes 0.083 ML. For an accurate description of the excess electrons produced by the V_O, DFT+U theory[69] is used with U applied to the Ti 3d electrons within a local spin density approximation. A 4.1 eV U value is adopted as it was found to adequately reproduce the work function, $W = 5.2$ eV,[70] and location of defect states at 0.9 eV below conduction band.[71]

3. RESULTS AND DISCUSSION

3.1. STM Studies of Low CO_2 Coverages. Previous experiments have shown that CO_2 initially binds to V_O sites and, as the coverage increases beyond that of V_O's, it starts to populate Ti_{5c} sites.[25,34,35,41] Our coverage-dependent STM measurements presented in Figure 1 lead to the same conclusion. The same area on TiO_2 (110) (Figure 1A,B) reveals new bright features resulting from the CO_2 adsorption in the location of the original V_O's. Very mild imaging conditions (1−2 pA) were used to prevent CO_2 reduction under the STM tip.[25,34,41] On the basis of the fraction of covered V_O's (each by a single CO_2), we determine the CO_2 coverage to be 0.06 ML. This quantity is further used to calibrate the CO_2 adsorption flux and to determine the CO_2 coverages in high coverage regime discussed below.

After saturation of V_O's, additional CO_2 adsorbs on Ti_{5c} rows. Following the same area as in Figure 1A,B, we show surfaces with 0.12 and 0.18 ML of CO_2 in Figure 1C,D, respectively. Both STM images exhibit streaks along the Ti_{5c} rows with the streak density increasing with increasing CO_2 coverage. We interpret the streaks as being a result of CO_2 diffusion at the rates that are much higher than the STM scanning rate resulting in multiple detection of the same molecule along the diffusion path. A similar conclusion has been reached in the previous study by Tan et al. where even imaging at 15 K did not immobilize CO_2 molecules on Ti_{5c} rows.[34]

To further investigate the behavior of CO_2 on ideal Ti_{5c} rows, we have prepared defect-free regions on the TiO_2 (110) using a high bias (~3 V) scan of the surface with CO_2 adsorbed in the V_O sites. As reported previously,[25,34,41] this procedure
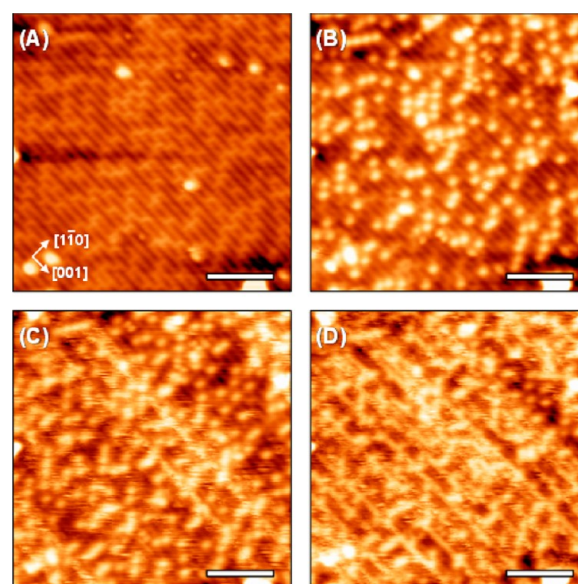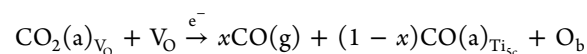

Figure 1. Same area STM images (1.3 V, 2 pA) obtained at 50 K from (A) clean TiO_2(110) and (B), (C), and (D) TiO_2(110) after adsorption of 0.06, 0.12, and 0.18 ML of CO_2, respectively. The scale bars correspond to 5 nm.

leads to electron-induced CO_2 reduction and oxidation of TiO_2(110) surface according to the following reaction:

$$CO_2(a)_{V_O} + V_O \xrightarrow{e^-} xCO(g) + (1 - x)CO(a)_{Ti_{5c}} + O_b$$

and results in the healing of V_O defects. We find that most of the CO desorbs ($x \cong 0.9$) but a small fraction ($1 - x \cong 0.1$) remains adsorbed on Ti_{5c} sites. An STM image obtained after this procedure and additional adsorption of 0.05 ML of CO_2 is shown in Figure 2A. The complete sequence of all the images obtained in the course of preparation of this surface is shown in Figure S2 (Supporting Information).

In comparison with the streak features on the reduced TiO_2(110), the pattern observed on an oxidized surface appears regular, and clearly show small, paired, bright, periodic features that form extended "tracks" along the Ti_{5c} rows (in Figure 2A highlighted with blue dots). Like the streaks seen in Figure 1C,D, the tracks in Figure 2A are likely to originate from the fast diffusion of CO_2 molecules. The area of Ti_{5c} rows covered by these features is much higher than the coverage of CO_2 molecules suggesting that each track in the STM image is a time average of CO_2 binding configurations being explored by rapidly diffusing CO_2. Similar tracks have also been observed on defect-free regions of reduced TiO_2(110) as illustrated in Figure S3 (Supporting Information). The absence of the ordered pattern on reduced TiO_2(110) is possibly caused by the structural and electronic perturbations introduced by V_O defects that smear out small energy differences between various CO_2 configurations (Figure S1, Supporting Information, and further discussion in section 3.2). Another type of feature observed in Figure 2A is the large bright protrusion centered on Ti_{5c} sites, which can be assigned to CO molecules produced by CO_2 reduction, in agreement with the previous studies of tip-induced CO_2 dissociation.[25,34,41] The CO_2 tracks are always terminated at the immobile CO molecules and/or step edge but not in the middle of the unhindered Ti_{5c} rows further indicating that they are a result of imaging highly mobile CO_2 molecules.
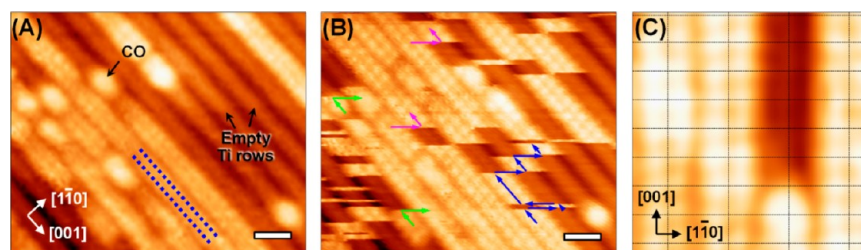
Figure 2. (A) STM image (1.3 V, 2 pA) from $TiO_2(110)$ after local V_O removal by tip induced CO_2 reduction (see text for details) and adsorption of additional 0.05 ML of CO_2 at 50 K. The large bright Ti_{5c}-centered features are CO molecules that in some cases remain on the surface after tip-induced CO_2 reduction on V_O's. The tracks of paired features, as indicated by the blue dots, are a result of imaging the rapidly diffusing CO_2. (B) Same as (A) imaged using I = 20 pA. Arrows indicate the STM tip induced CO_2 cross-row transfer. The scale bars in (A) and (B) correspond to 1 nm. (C) High magnification area from (A) superimposed with a grid indicating Ti_{5c} positions.

Further evidence for the CO_2 diffusion along the Ti_{5c} rows is provided in Figure 2B where the same area was scanned with higher tunneling current (I = 20 pA, scan in the image is directed horizontally). Frequently, the CO_2 track shifts from one Ti_{5c} row to another as indicated with blue arrows in several places. This shift is a result of a tip-mediated transfer of CO_2 across the O_b row to a neighboring Ti_{5c} row and provides clear evidence for the track being an image of a single CO_2 molecule diffusing rapidly along the Ti_{5c} row. Tracks can also disappear and/or appear suddenly without any apparent changes in neighboring Ti_{5c} rows likely indicating CO_2 transfers to and/or from a row occupied by more than one CO_2 (Figure 2B, green and magenta arrows, respectively). In some cases, the appearance/disappearance of the tracks could also be caused by CO_2 transfer from and/or to the STM tip.

An additional high magnification image of the CO_2 tracks is presented in Figure 2C. The positions of the surface Ti_{5c} ions are overlaid (black grid) with the image to indicate the positions of the maxima with respect to the underlying Ti_{5c} lattice. The overlay clearly shows that the pairs of bright maxima are always centered above the positions of Ti_{5c} ions.

The tip-induced CO_2 transfer across the O_b rows observed in Figure 2B raises questions about the tip-induced effects even under mild scanning conditions used in Figure 2A. Though our current- and bias-dependent images do not show any significant differences in the appearance of the observed CO_2 tracks, the fact that the feature intensities are independent of the number of CO_2 molecules on the row and the track length can be only explained by invoking attractive tip–CO_2 interactions. The equal intensities indicate that the CO_2 diffusing along Ti_{5c} rows is stabilized under the tip as it passes over the Ti_{5c} row and is again released as the tip continues scanning across the O_b row. In case of higher tunneling current (resulting in a smaller tip–surface distance), the further enhanced attractive tip–CO_2 interactions facilitate CO_2 transfer across the O_b rows as shown in Figure 2B.

3.2. Theoretical Studies of CO_2 Binding and Diffusion on Ti_{5c} Rows at Low Coverages. To explain the appearance of CO_2 related features in the STM images and understand CO_2 adsorption at low coverages, a number of CO_2 binding configurations were investigated using dispersion-corrected DFT calculations. The low energy configurations relevant for the discussion presented here are shown in Figure 3A. Additional configurations and their relative binding energies are presented in Figure S1 (Supporting Information).

In the energetically most stable configuration ("r1", see Figure 3A), CO_2 is bonded with one O atom, denoted O_a, on top of a Ti_{5c} site with the long O=C=O bond axis tilted at a polar angle, $\psi \cong 45°$ with respect to surface normal along the $[1\bar{1}0]$

direction (azimuthal angle, φ = 90°) toward one of the closest O_b ions. Our calculated binding energy in this configuration is 0.45 eV relative to gas phase CO_2 and bare $TiO_2(110)$, in good agreement with the DFT values of 0.44 (PBE-TS functional) and 0.39 eV (PBE-D) reported by Sorescu et al.[35] For configuration "r2" (Figure 3A) the tilted CO_2 is rotated azimuthally to φ = 45° and the relative energy increases only slightly (ΔE = 0.02 eV), suggesting that azimuthal CO_2 rotation about the Ti_{5c}–O_a axis may be facile. In configuration "r3" (Figure 3A, ΔE = 0.03 eV) the CO_2 adsorbs parallel to the surface (ψ = 90°, φ = 0°) with each oxygen bound at the distance of 2.33 Å to two neighboring Ti_{5c} sites.

Calculations of the reaction paths for both translation along the Ti_{5c} row (Figure 3B) and rotation about the Ti_{5c}–O_a axis (Figure 3C) support the hypothesis that diffusion is facile even at low temperatures. This is consistent with the fast CO_2 diffusion observed both on reduced and oxidized $TiO_2(110)$, as discussed in the previous section. For diffusion along the Ti_{5c} row we consider a combined rotation/tumbling pathway where CO_2 starts in configuration r1 rotates about O_a to r2, then through a transition state (TS1, Figure 3B) to r3. From r3 the molecule can reverse the process to end up back where it started. Alternatively, if the molecule switches its anchoring oxygen atom while in r3, then the next transition to r1 moves it one site along the Ti_{5c} row. This process exhibits an energy barrier of only 0.06 eV (Figure 3A, TS1), suggesting that it will be extremely rapid even at very low temperatures. This diffusion along the rows is competitive with rotation about the Ti_{5c}–O_a axis, which requires only 0.05 eV for rotation between two symmetrically equivalent lowest energy minima that are related by a rotation about the Ti_{5c}–O_a bond by 180° (Figure 3C). The same is not true for diffusion between Ti_{5c} rows, where the barrier is found to be approximately 0.21 eV (data not shown). Thus it is anticipated that diffusion along the Ti_{5c} row will be the dominant process. Finally, it is noted that these results are in good accord with the recent combined STM/DFT study by Lee et al.[24]

3.3. STM Studies of High CO_2 Coverages. In this section we focus on the STM results obtained by imaging CO_2 at coverages ranging from 0.5 to 1 ML. The representative STM images from as-prepared CO_2 overlayers following the dose at 50 K are shown in Figure 4A. Figure 4A(a) shows $TiO_2(110)$ after a 0.58 ML dose of CO_2 at 50 K. The underlying structure defined by alternating Ti_{5c} and O_b rows can be recognized in the image but no long-range order in the CO_2 overlayer is observed. In some areas (highlighted by blue dotted rectangles), the small, bright, paired features resembling those observed at low coverages can be recognized (Figure 2).

Figure 4A(b) shows an STM image at θ = 0.74 ML that approximately corresponds to two CO_2 molecules per three Ti_{5c}
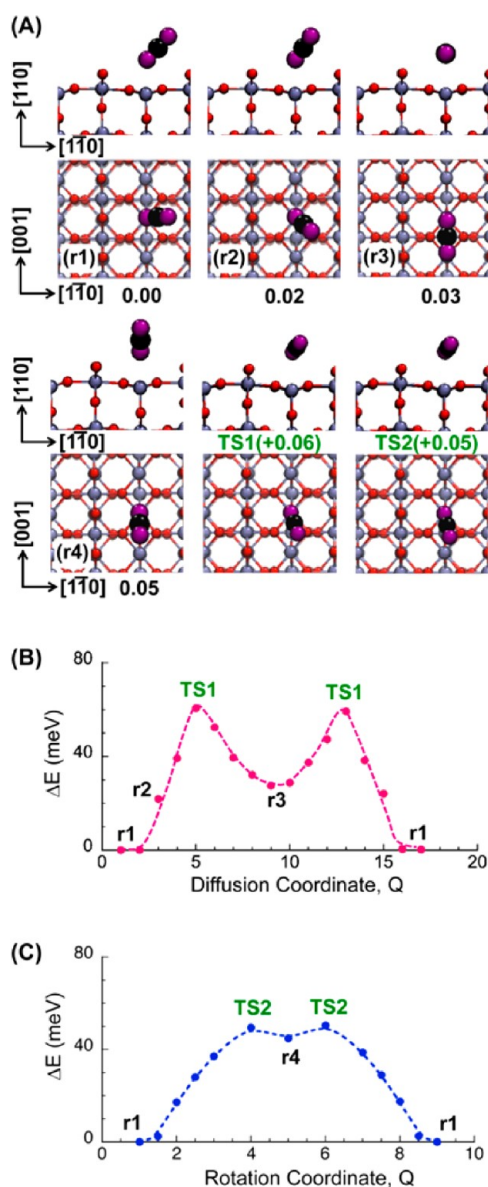
Figure 3. (A) (r1–r4) Selected low energy binding configurations for CO_2 on Ti_{5c} sites of $TiO_2(110)$; relative energies with respect to the lowest energy configuration, r1, are quoted in electronvolts below each configuration. A more extensive set is provided in Figure S1 (Supporting Information). (TS1, TS2) CO_2 configurations at transition states TS1 and TS2 along the diffusion and rotation coordinate shown in (B) and (C), respectively. (B) Energy profile (in meV) along the CO_2 diffusion coordinate with relevant configurations and their energies given in (A). (C) Energy profile along the CO_2 rotation coordinate about Ti_{5c}–O_a axis with relevant configurations and their energies given in (A). For (B) and (C) data points indicate energy of the replicas along the diffusion/rotation coordinates obtained from CI-NEB and line is a guide to the eye.

sites (after accounting for the CO_2 adsorbed in Vo's). In contrast with the 0.58 ML image in Figure 4A(a), the paired features can be discerned across most of the surface. Several particularly well-ordered areas are highlighted by blue dotted rectangles. Interestingly, the spacing of the double dotted features along the Ti_{5c} rows is ~1.5 times larger than the spacing of the Ti_{5c} ions. We will further return to this observation below.

An image after adsorption of 1.08 ML of CO_2 corresponding to one CO_2 per one Ti_{5c} is shown in Figure 4A(c). Although

the image shows some disorder due to perturbations by V_O defects, zigzag arrangements of small features along the Ti_{5c} row can be clearly discerned. The bright features have 2× periodicity along the Ti_{5c} row and are out-of-phase across the O_b row forming an overlayer with (2 × 2) periodicity. Interestingly, this configuration is similar to that proposed for N_2 on $TiO_2(110)$ by Rittner et al.[72] and is also consistent with experiments for a number of weakly bound molecules such as N_2, O_2, and CO.[48,73]

To evaluate how the order of the CO_2 overlayers changes in the absence of V_O's, we again use high bias ($U = 3$ V) scan to oxidize the surface. The same areas of the as-dosed over-layers (Figure 4A(a–c)) after the V_O removal are shown in Figure 4B(a–c). The images demonstrate that the V_O removal leads to increase of the order in the CO_2 overlayers. The bottom panels in Figure 4B are magnified areas from the top panels overlaid with proposed structural models of CO_2 on $TiO_2(110)$.

The most dramatic changes are observed at 0.58 ML, Figure 4B(a), where the highly disordered overlayer is converted to highly ordered one, with the paired features covering most of the surface. The features are ordered with respect to the underlying $TiO_2(110)$ and exhibit 1 × 1 periodicity. The appearance of these features is analogous to those observed in Figure 2. A number of defects, likely due to the presence of bridging hydroxyl (HO_b) impurities and $CO(a)_{Ti_{5c}}$ from tip-induced CO_2 dissociation can also be recognized. Though the image shows a paired feature on each Ti_{5c} site, there can only be one CO_2 per every two Ti_{5c} sites based on the amount of CO_2 dosed. This indicates that CO_2 remains fairly mobile on oxidized surface at this coverage and the image represents the time average of diffusing CO_2 molecules similarly with the low coverage regime images discussed in the previous sections. A magnified view of the tracks superimposed with the model of diffusing CO_2 molecules dynamically switching between two equivalent configurations on each Ti_{5c} site is schematically shown in Figure 4B(d). On the basis of the model presented below and the distances between the two bright maxima (along $[1\bar{1}0]$ direction, $\varphi = 90°$) on top of each Ti_{5c} site, we estimate the tilt angle of the CO_2 with respect to the surface normal to be $\psi = 35 \pm 5°$.

At $\theta = 0.74$ ML (Figure 4B(b)), the V_O removal also results in the development of ordered overlayer. In contrast with the 0.58 ML (Figure 4B(d)) where the paired features are aligned with the underlying Ti_{5c} ions, the spacing of the paired features at 0.74 ML (Figure 4B(b)) is ~4.5 Å along the Ti_{5c} rows, which is approximately 1.5 times that of the Ti_{5c}–Ti_{5c} distance of 2.95 Å. These arrangements are similar to the ordered areas highlighted with the blue rectangles on the as prepared overlayer (Figure 4A(b)). Interestingly, the paired features are offset from one Ti_{5c} row to the next. These differences indicate that the CO_2 molecules bound on neighboring Ti_{5c} sites are most likely tilted away from each other as schematically shown in high magnification image in Figure 4B(e) due to the steric repulsion between adjacent CO_2 molecules. Additionally, the fact that the positions of the spots with respect to the underlying Ti_{5c} sites do not change from image to image (not shown) indicates that the CO_2 diffusion along the Ti_{5c} rows is hindered. The model superimposed on top of the image yields a CO_2 orientation with an azimuth of $\varphi = 55 \pm 10°$ and tilt of $\psi = 42 \pm 5°$.

At $\theta = 1.08$ ML (Figure 4B(c,f)), only slight increase in the order of the zigzag structure as compared to the as prepared

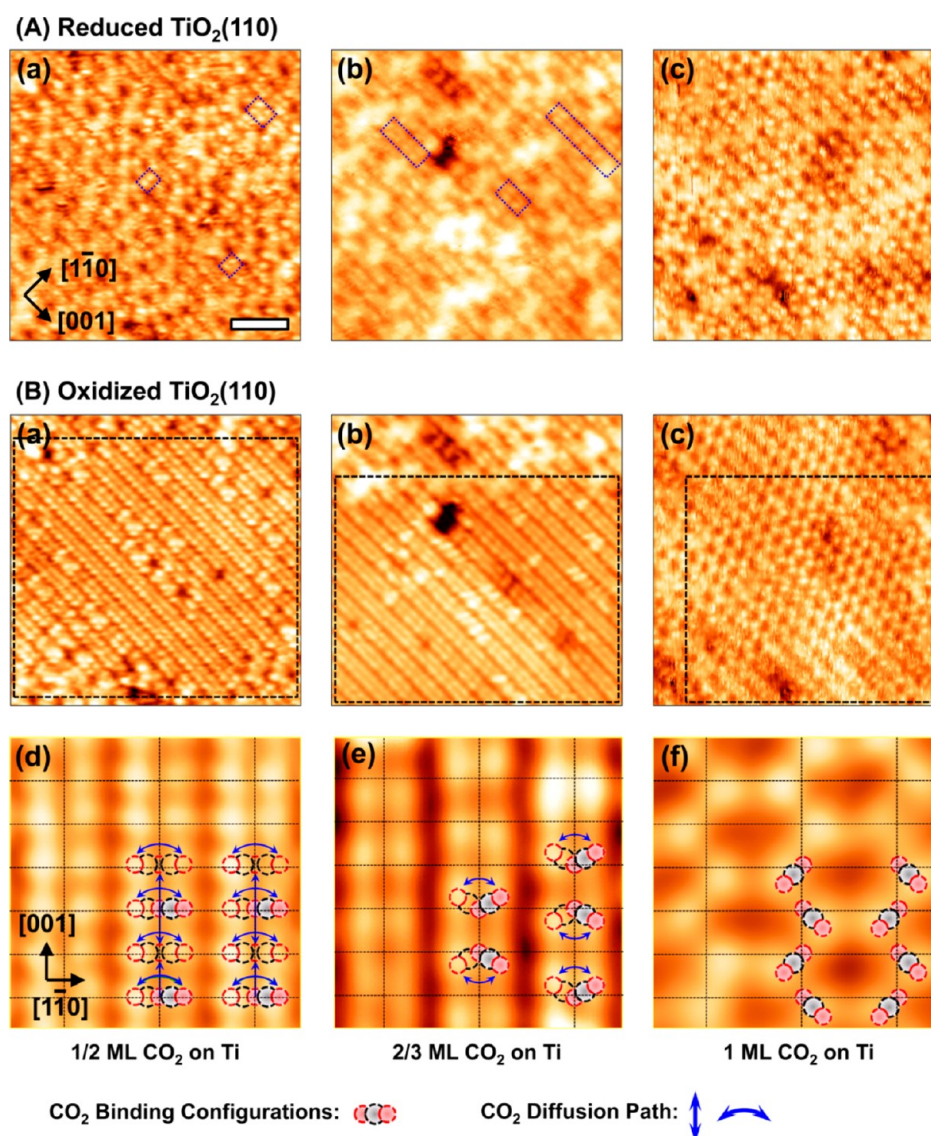**Figure 4.** STM images (1.3 V, 10−15 nA) from CO_2 overlayers adsorbed on $TiO_2(110)$ at 50 K. (A) shows as prepared surfaces with coverages of 0.58 (a), 0.74 (b), and 1.08 ML (c). (B) Images (a)−(c) show the same surface area after additional high bias scan (3 V, black rectangles indicate the area treated) leading to V_O removal (see text for details). The scale bar in A(a) corresponds to 2 nm in the images shown in A(a−c) and B(a−c). Panels B(d−f) show high magnification images from the areas scanned with high bias. The images are overlaid with the models representing time average of the configurations sampled by CO_2 during STM imaging. The models are derived on the basis of STM, IRAS, and DFT data presented in this publication. The grid dotted lines in B(d) correspond to the positions of Ti_{5c} ions derived from the STM image. STM images in B(e) and (f) allow only the identification of Ti_{5c} rows, but not the individual sites. Therefore, the positions of grid lines along [001] direction are based on the models derived on the basis of STM, IRAS, and DFT.

overlayer (Figure 4A(c)) is seen. The stability of this structure in the presence of V_O's indicate that the energy gained by this arrangement is higher than the perturbations introduced by the surface V_O's.

3.4. Coverage-Dependent TPD Studies. To determine the absolute CO_2 coverages on different adsorption sites (V_O's, Ti_{5c}'s, and O_b's) and the corresponding CO_2 binding energies, we have performed molecular beam scattering and TPD studies. Measurements of the coverage-dependent sticking coefficient using the King and Wells technique[74,75] with a calibrated CO_2 flux[76] show that the initial sticking coefficient of CO_2 on $TiO_2(110)$ is high ($S_0 = 0.98$) and quickly approaches unity with increasing coverage (Figure S4, Supporting Information).

TPD spectra as a function of CO_2 coverage are shown in Figure 5 (essentially identical results are obtained on both the

IRAS and MB systems, Figure S5, Supporting Information). Three peaks observed at ~122, ~139, and ~163 K can be assigned to CO_2 bound directly on different surface sites on $TiO_2(110)$. The additional peak at ~75 K indicates the onset of multilayer desorption at higher CO_2 coverages. The observed peak positions are in agreement with previously reported TPD spectra.[10,11] The desorption energies at the highlighted peak desorption temperatures were determined using an inversion analysis that assumes first-order desorption kinetics.[75,77] The complete coverage dependence of CO_2 desorption energies is shown in Figure S6 (Supporting Information).

In previous studies, the small TPD peak at ~163 K was assigned to CO_2 desorption from V_O's.[10,11] This is consistent with our STM experiments that show that at low coverages CO_2 preferentially adsorbs on V_O sites (Figure 1). However, quantitative analysis of our TPD data reveals that the amount of
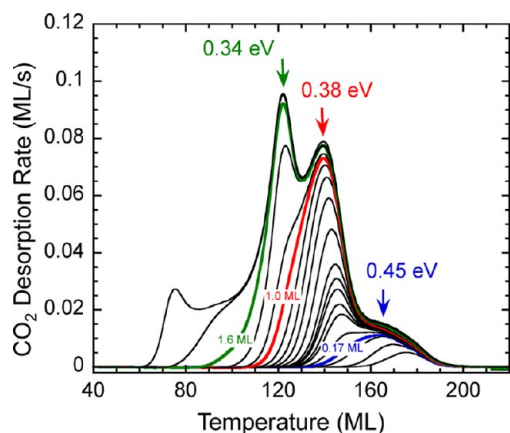
Figure 5. CO_2 TPD spectra for several coverages for CO_2 dosed on reduced $TiO_2(110)$ at 25 K obtained using a ramp rate of 2 K/s. Bold blue, red, and green traces correspond to $\theta = 0.17$, 1.0, and 1.6 ML, respectively. The coverage-dependent desorption activation energies, which are shown for the marked TPD peaks, are determined using an inversion analysis that assumes first-order desorption kinetics.[75,77] The optimized value of the preexponential factor determined from the inversion analysis is $1 \times 10^{13\pm2}$ s^{-1}. The relative error of the energy determination is estimated to be ±15% (Figure S6, Supporting Information).

CO_2 in the 163 K TPD peak is ~0.17 ML, which is ~3 times higher than the V_O concentration (~0.053 ML, based on the analysis of water TPD spectra).[50,51]

As the CO_2 coverage is increased above 0.17 ML, a TPD peak develops at 145 K and shifts to slightly lower temperatures with increasing CO_2 coverage. This peak corresponds to CO_2 adsorption on Ti_{5c} sites in accord with previous assignments,[10,11] and our STM experiments presented in Figures 3 and 4. This peak saturates at ~1.0 ML of total CO_2 coverage indicating that one CO_2 occupies each Ti_{5c}.

For coverages greater than 1 ML, a third TPD peak appears at 122 K due to CO_2 adsorption on O_b sites (Figure 5). This TPD peak saturates at a CO_2 coverage of ~1.5 ML and corresponds to the same coverage observed previously for CO, O_2, and N_2 adsorption on $TiO_2(110)$.[48] The adsorption of up to 0.5 ML on the O_b sites is the result of a specific adsorption configuration of CO_2 on the Ti_{5c} rows. This binding configuration was first proposed in theoretical calculations for N_2 on $TiO_2(110)$[72] and is imaged in Figure 4A(c). The molecules on Ti_{5c} sites are tilted in a zigzag fashion from the surface normal toward neighboring O_b rows to minimize repulsion and are arranged out of phase from one Ti_{5c} row to the next. Because this tilted configuration blocks half of the O_b sites, it allows for an additional 0.5 ML adsorption of CO_2 on top of O_b's.

It should be noted that a desorption temperature of 122 K corresponds to a binding energy of 0.34 eV for CO_2 on the O_b sites, which is only ~10% lower than the CO_2 binding energy on Ti_{5c} sites. However, previous calculations predicted this adsorption energy would be 43% lower.[35] This apparent discrepancy is due to the fact that the calculations for CO_2 on O_b were carried out in the absence of CO_2 adsorbed on the Ti_{5c} sites. As discussed in section 3.7, the strong quadrupole–quadrupole interactions with the nearby Ti_{5c}-bound CO_2 molecules increase the CO_2 binding energy on the O_b sites.

3.5. Coverage-Dependent IRAS Studies. We also investigated the adsorption of CO_2 on $TiO_2(110)$ using azimuth- and polarization-resolved IRAS. For all coverages, and both polarizations and azimuthal orientations, the only CO_2 vibrations detected were due to the asymmetric stretch of

neutral CO_2. Only slight shifts of the vibrational frequency from the gas phase value (2349 cm^{-1}) were detected, indicating that adsorption on $TiO_2(110)$ causes little change in the electronic structure of the CO_2. These general observations are consistent with the other experimental results and the calculations presented here. In addition to identifying the species involved, using both s- and p-polarized light with the IR beam incident along either the [001] or [1$\bar{1}$0] azimuths provides information about the (ensemble-averaged) adsorption geometry of the adsorbed CO_2.

Figure 6 shows the s-polarized IRAS spectra for the asymmetric stretch of CO_2 for coverages up to 1 ML. For all coverages,
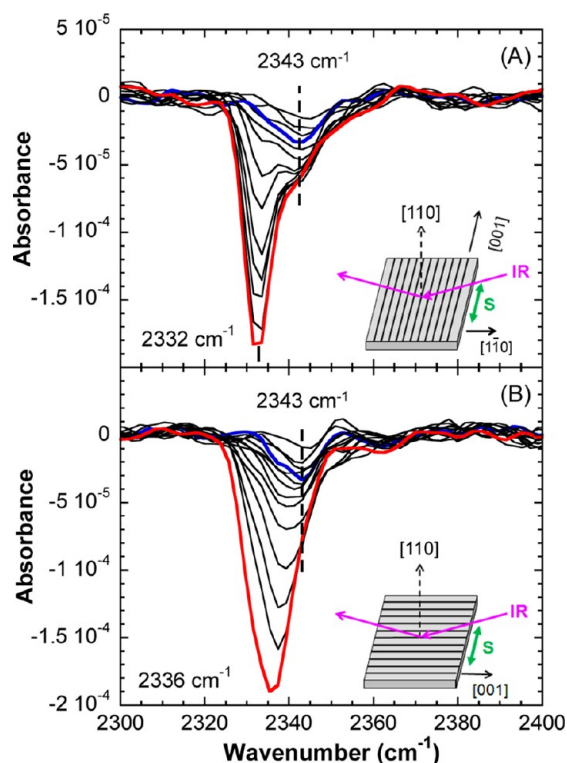

Figure 6. S-polarized FTIR spectra from CO_2 on $TiO_2(110)$ as a function of coverage ($\theta = 0 - 1$ ML) acquired at 25 K. The IR beam is directed (A) along [1$\bar{1}$0] and (B) along [001] azimuth of the $TiO_2(110)$ surface (see the illustrations). Bold blue and red traces correspond to coverages that saturate the 163 and 139 K peaks in the TPD spectra in Figure 5, respectively.

negative absorbances are seen, as expected for an adsorbate on a dielectric substrate.[78−80] For s-polarized light with the IR beam parallel to the [1$\bar{1}$0] azimuth ($\varphi = 90°$, Figure 6A), the measurement is sensitive to vibrations that are parallel to the surface and parallel to the O_b rows, they look better resolved. Conversely for the [001] azimuth ($\varphi = 0°$, Figure 6B), the measurement is sensitive to vibrations parallel to the surface but perpendicular to the O_b rows, they look less resolved. For both azimuths, a peak at ~2343 cm^{-1} develops at the lowest CO_2 coverages and saturates at 0.17−0.20 ML coverage, as seen in Figure 6. This coverage is close to the saturation coverage for the 163 K peak in the CO_2 TPD spectra (Figure 5). The spectra marked with blue lines correspond to the coverage (~0.17 ML) that saturates the CO_2 TPD peak at ~163 K. For larger CO_2 coverages, the spectra for the [1$\bar{1}$0] azimuth begin to develop a new peak at ~2332 cm^{-1} (Figure 6A). For the [001] azimuth, the absorbance also increases and the peak shifts to lower frequency with increasing CO_2 coverage (Figure 6B). The spectra marked
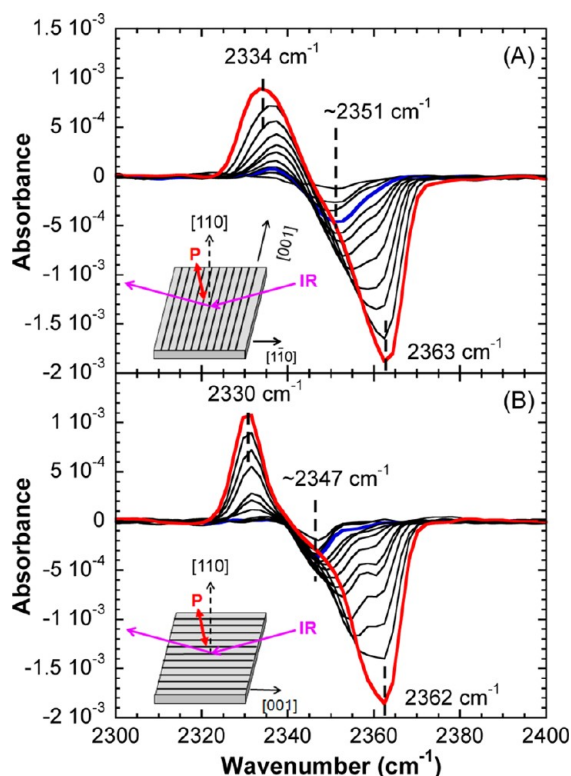
Figure 7. P-polarized FTIR spectra from CO_2 on $TiO_2(110)$ as a function of coverage ($\theta = 0-1$ ML) acquired at 25 K. The IR beam is directed (A) along $[1\bar{1}0]$ and (B) along $[001]$ azimuth of the $TiO_2(110)$ surface (see the illustrations). Bold blue and red traces correspond to coverages that saturate the 163 and 139 K peaks in the TPD spectra in Figure 5, respectively.

with red lines in Figure 6 correspond to 1 ML CO_2 coverage (i.e., the coverage that saturates the TPD peak at ~139 K; Figure 5, red line).

Figure 7 shows the p-polarized spectra for CO_2 coverages up to 1 ML. Panels A and B of Figure 7 show the spectra for the IR beam along the $[1\bar{1}0]$ and $[001]$ azimuths, respectively. For p-polarized light the electric field has components both parallel and perpendicular to the surface. Thus, the measurement is sensitive to vibrations normal to the surface, and parallel to the surface in the direction of the IR beam. For coverages up to 0.17 ML, the spectra from both azimuths show a single negative absorbance at ~2351 and 2347 cm^{-1} for the $[1\bar{1}0]$ and $[001]$ azimuths, respectively. As the CO_2 coverage increases, the negative absorbance peak shifts to higher frequencies and a positive absorbance peak at lower frequencies emerges.

For p-polarized spectra on a dielectric surface, the sign of the absorbance is related to the orientation of the transition dipole moment responsible for the absorbance: Positive absorbances arise from vibrations that have a component parallel to the surface whereas negative absorbances arise from vibrations that have a component perpendicular to the surface.[79,81] Therefore, the negative absorbances seen at all coverages in Figure 7 indicate that the ensemble of adsorbed CO_2 has a component normal to the surface for all coverages shown.

The evolution of the p-polarized spectra as a function of CO_2 coverage (Figure 7) can be understood qualitatively in terms of dipole−dipole coupling within the adsorbate layer.[79,81,82] At low coverages, dipole−dipole coupling is relatively weak and the adsorbate layer absorbs IR light at a single frequency associated with an isolated CO_2 adsorbed on $TiO_2(110)$. As the

CO_2 coverage increases, the dipole−dipole coupling increases. The coupling shifts the negative absorbance in the p-polarized spectra to higher frequencies but has a smaller effect on the positive absorbance peak. (An alternative description of this phenomenon is that as the absorption increases due to the increasing coverage, the magnitude of the anomalous dispersion increases and eventually splits the absorbance into positive and negative components.)

STM images indicate that at the lowest coverages CO_2 preferentially adsorbs in V_O's (Figure 1A, B), but the TPD results (Figure 5) show that the 166 K feature in the spectra continues to grow following the saturation of V_O sites and therefore cannot be attributed solely to a single CO_2 occupying V_O site. To explore this issue further, we have obtained a small set of IRAS spectra at higher resolution ($\Delta\nu = 1$ cm^{-1}) and small CO_2 coverages. (At this resolution, the spectra take considerably longer to acquire, making it difficult to obtain a large data set.)

Figure 8 shows s-polarized spectra with the IR beam parallel to the O_b rows for $\theta \cong 0.03$, 0.07, and 0.14 ML. For $\theta \cong 0.03$ ML,
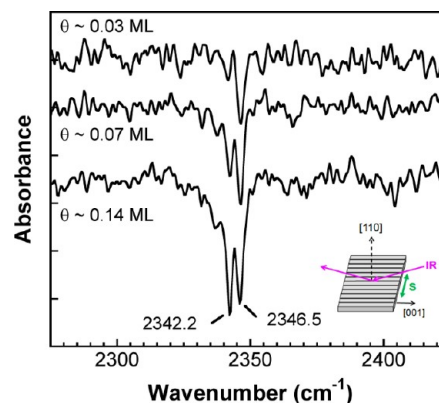

Figure 8. IRAS spectra for s-polarized light incident parallel to the $[001]$ azimuth of $TiO_2(110)$, with a resolution of $\Delta\nu = 1$ cm^{-1}. At this higher resolution, two peaks are resolved at intermediate coverages (0.03 to 0.14 ML). On the basis of STM results, the peak at $\nu = 2346.5$ cm^{-1} is due to CO_2 adsorbed in the V_O sites.

all the CO_2 should be adsorbed in V_O's and the spectrum has a single peak at 2346.5 cm^{-1}. For $\theta \cong 0.07$ ML, the CO_2 coverage is greater than the V_O concentration. In this case, the peak at 2346.5 cm^{-1} is slightly larger, and a new peak at 2342.2 cm^{-1} has appeared, indicating a new adsorption site is being populated. The peak at 2342.2 cm^{-1} continues to grow until $\theta \cong 0.14$ ML (i.e., approximately at the saturation of the highest temperature feature in the TPD spectra for this sample). For the corresponding p-polarized spectra with $\Delta\nu = 1$ cm^{-1}, a single, narrow peak at 2346.5 cm^{-1} also saturates when the CO_2 coverage is approximately equal to the V_O coverage (data not shown). On the basis of these data, the peak at 2346.5 cm^{-1} is assigned to CO_2 adsorbed in V_O's, whereas the peak at 2342.2 cm^{-1} presumably arises from CO_2 adsorbed on the Ti_{5c} rows. This issue is further addressed in the following section using DFT calculations.

The IRAS spectra provide important information about the orientation of the adsorbed CO_2 on Ti_{5c} sites. Specifically, the IR spectra in Figures 6 and 7 reflect projections of the ensemble-averaged molecular orientation on the $[110]$, $[1\bar{1}0]$ and $[001]$ azimuths. The slopes of the integrated absorbance for the s-polarized spectra versus CO_2 coverage are similar (within 15% error) for both the $[1\bar{1}0]$ and $[001]$ azimuths, indicating that the ensemble-average of adsorbed CO_2 has

approximately equal components along both azimuths. Further, the p-polarized spectra clearly indicate that the ensemble-average for the CO_2 has a component normal to the surface. The ensemble-averaged orientation may represent a single (or dominant) adsorption geometry with molecular axis oriented ~45° with respect to the [001] direction, or combination of several adsorption geometries (for example, Figure 3). For lower CO_2 coverages ($\theta < 0.5$ ML), the IRAS results are in good agreement with the rotating-tumbling diffusion of the molecules along the Ti_{5c} row, which follows from the DFT calculations (Figure 3) and STM images in the presence of V_O's (Figure 1). For higher CO_2 coverages ($\theta = 2/3$ and 1 ML), the "diffusion streaks" disappear from the STM images replaced by more structured adsorbate layers, where the molecules have preferred orientations relative to each other and to the substrate lattice. For such systems, the IRAS spectra may correspond to a single (or dominant) adsorption geometry for the CO_2 that is tilted with respect to the surface normal and rotated ~45° relative to the O_b rows.

3.6. Theoretical Studies of V_O Defect Site Effect on CO_2 Binding.
As noted above there are three main desorption features present in the coverage dependent TPD spectra of Figure 5; the first at 122 K assigned to CO_2 bound at O_b sites, the second at 139 K assigned to CO_2 bound at the Ti_{5c} sites, and the third at 163 K in part due to adsorption in V_O defect sites and in part due to more stable CO_2 configurations on Ti_{5c} rows. This third feature is also represented by a separate IR peak near 2343 cm^{-1} (Figure 6A) and the nature of this feature is not quite clear. In this section we theoretically investigate CO_2 adsorption on $TiO_2(110)$ surface with V_O defects, trying to understand adsorbate configurations with higher binding energy.

To properly account for the distribution of the charge that is formed as a result of V_O formation,[83] we apply the DFT+U method to determine the CO_2 configuration and binding energy in the V_O site. The binding energy value is found to be 0.60 eV, which is 0.17 eV higher than the CO_2 binding on a regular Ti_{5c} site. This is in agreement with the STM measurements (Figure 2) that show V_O as a preferential CO_2 adsorption site.

We have also calculated the binding energy of a CO_2 adsorbed next to a CO_2 bound in a V_O site (Figure S7, Supporting Information). In this case, the CO_2 binding energy is 0.48−0.49 eV which is 0.05−0.06 eV higher relative to CO_2 binding on regular Ti_{5c} sites. As shown in Figure S7 (Supporting Information), the lowest energy configurations show that the Ti_{5c} bound CO_2 interact with those at V_O via either T-shaped or slipped-parallel quadrupole−quadrupole CO_2−CO_2 interactions similar to those seen in the liquid CO_2 phase.[63,84,85] The binding energies of these two species associated with the V_O defects do not overlay perfectly with the TPD data for the 163 K feature, but qualitatively the results indicate that introducing V_O defects opens an additional broad envelop of desorption energies, which are higher than those seen on isolated Ti_{5c} sites. This may provide an explanation for the high temperature peak observed in TPD (Figure 5); however, such more tightly bound CO_2 molecules in the vicinity of CO_2 filled V_O's are not observed in the STM images (Figure 1), possibly because even the more tightly bound Ti_{5c}-bound CO_2 remains mobile.

3.7. Theoretical Studies of Coverage-Dependent CO_2 Binding Configurations.
To understand the adlayer structure at higher coverages, we have undertaken AIMD simulations at coverages of 1/3, 1/2, 2/3, and 1 ML. The simulations are performed at $T = 130$ K (i.e., near the desorption temperature) to maximize our ability to sample the available configuration space within the short (20 ps) duration of AIMD trajectories. In this

short time, we are able to see CO_2 rotation and diffusion events, but not desorption events.

The CO_2 forms a dynamically disordered adlayer in the AIMD simulations for the coverages investigated. A representative set of configurations observed at different coverages are shown in Figure 9A. To assess the energy differences between
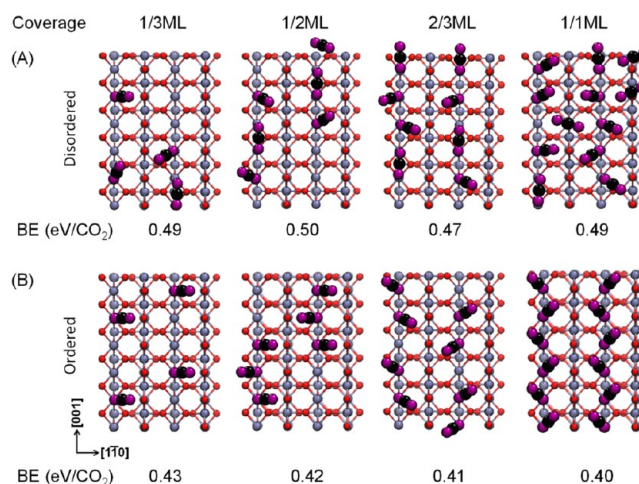

Figure 9. (A) Representative snapshots of disordered configurations extracted from the 130 K AIMD runs have been quenched to $T = 0$ K. (B) Ordered configurations constructed on the basis of frequent motifs observed in AIMD simulations and images observed in STM experiments. The simulations are obtained by a slow annealing at $T = 50$ K.

the disordered configurations observed in the AIMD simulations and the ordered structures suggested by the periodic patterns observed in the STM images (Figures 2 and 4), we calculated the relative energies of the configurations extracted from our MD trajectories at $T = 0$ K and compare them with hypothetical ordered configurations (Figure 9B) observed in the STM images. The disordered configurations (Figure 9A) extracted from the 130 K AIMD runs have been quenched to $T = 0$ K whereas the ordered configurations (Figure 9B) are obtained by a slow simulated annealing simulation at $T = 50$ K to allow for the maximal structure optimization but suppress some of the higher energy interconversions seen at higher temperatures. Comparing the binding energies, the ordered configurations are found to be 0.06−0.09 eV/CO_2 less stable than the equilibrated dynamic configurations. Such energy differences are well within the kinetic energy distribution available at 100 K, but free energy effects would favor the disordered structures. It can thus be concluded that our AIMD simulations suggest that CO_2 films on TiO_2 are only partially ordered at all coverages.

From Figure 9A one can infer that the majority of CO_2 are bound with one O atom to a Ti_{5c} site and are tilted from the surface normal toward O_b rows in the configurations resembling those shown in Figure 3A(r1−r2). Additionally a non-negligible fraction is lying flat in the configurations resembling that in Figure 3A(r3). In general, the Ti_{5c}-bound CO_2 are almost free to rotate (barrier of 0.05 eV) about the Ti_{5c}−O_a axis and, in addition, they readily diffuse at low coverages whereas they become more restricted at high coverages. Unfortunately, the limited statistics from AIMD does not allow us to quantify the coverage dependence of the diffusion rates. However, even within the relatively short time (~20 ps) several CO_2 hopping motions along the Ti_{5c} rows are observed. For example, hopping is observed 0.125 times/ps/CO_2 at 1/3 ML
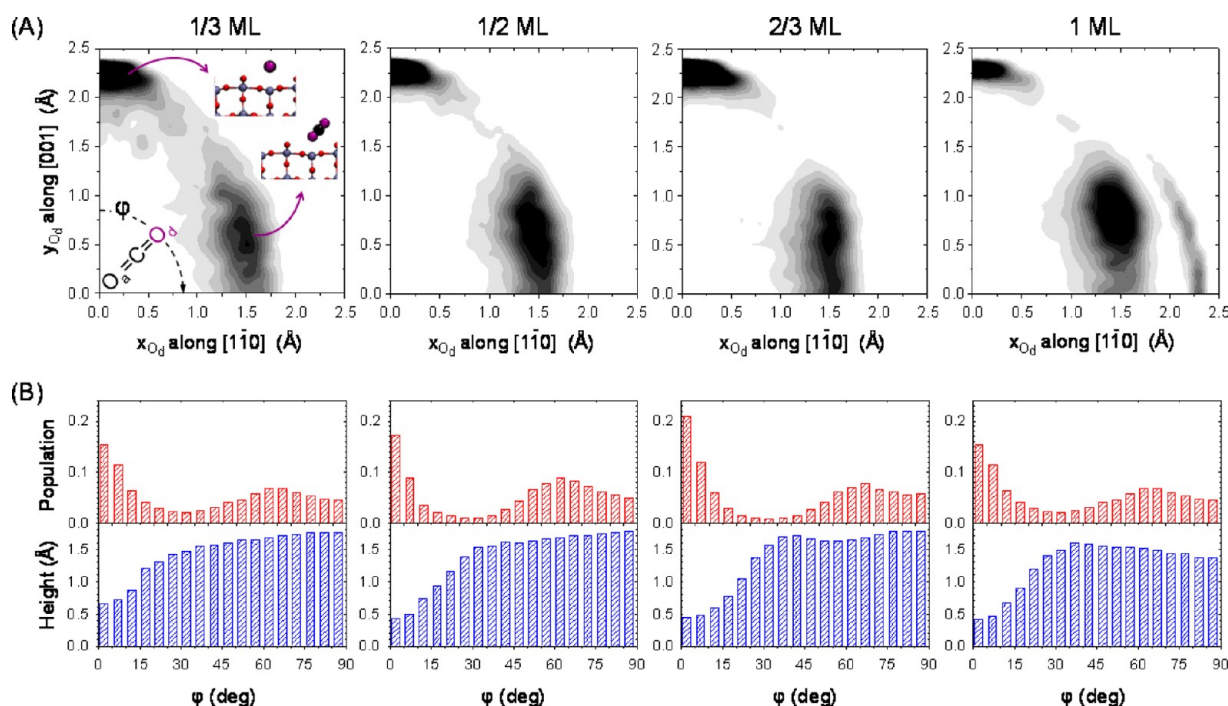
Figure 10. (A) Distributions of binding configurations (from the O_d projection onto the $TiO_2(110)$ surface plane) for all CO_2 molecules that are bound to Ti_{5c} obtained from AIMD simulations at 130 K. (B) Upper subpanels show probability distribution functions, $P(\varphi)$, as a function of azimuthal angle, φ (see text for definition). Lower subpanels show the average height of O_d above the anchored O_a atom of the molecule as a function of φ. Increasing coverages of 1/3, 1/2, 2/3, and 1 ML are shown from left to right.

whereas almost 10 times less hopping events are observed at 1 ML. Focusing on the low coverage of 1/3 ML, the Arrhenius formula assuming the preexponential factor of 1×10^{13} s^{-1} is used to estimate the hopping energy barrier of 0.06 eV, which is very close to the value of 0.05 eV determined in section 3.2. Therefore, the fast diffusion evidenced in the STM images (e.g., Figure 2) is also consistent with our current AIMD trajectories.

The above presented data characterize the observed CO_2 orientations; we now briefly discuss the CO_2 spacing by examining the distribution of O_a-O_a distances and O_d-O_d distances (O_d is the terminal, dangling O atom of the bound CO_2) observed in our AIMD simulations (Figure S8, Supporting Information). From the former quantity it is found that CO_2 is neighbored by another CO_2 approximately 63 and 75% of the time at 1/3 and 1/2 ML as compared to 44 and 75%, respectively, expected if the molecules were randomly distributed. This indicates that CO_2-CO_2 intermolecular interactions on the Ti_{5c} sites must be attractive. The distribution of O_d-O_d pairs for these neighboring molecules is broad at 1/3−1/2 ML coverage ranging between 1 and 2 lattice spacing (ca. 3−6 Å) with a maxima at ca. 5 Å indicating that the neighboring molecules prefer to orient away from each other.

At higher coverages, the first nearest neighbor pairing of CO_2 molecules is on the order expected from the coverage and the O_d-O_d distribution becomes sharper but retains a maximum value of 4.5−5.0 Å, which would result in a zigzag pattern reminiscent of the STM images in Figure 4A(c).

To further facilitate the comparison of the AIMD calculations with the coverage dependent STM images (Figures 2 and 4) and the azimuth-resolved IRAS spectra (Figures 6 and 7), we plot the distribution maps of CO_2 orientations obtained from the AIMD trajectories. Two dimensional (2D) distribution maps of the O_d positions (relative to the Ti_{5c} site where CO_2 is bound) projected onto the $TiO_2(110)$ surface plane are plotted in Figure 10. The molecules which do not have one of their O atoms within 2.5 Å

from any Ti_{5c} site (i.e., within the first nearest neighbor peak of the $Ti_{5c}-O_a$ radial distribution function) are excluded from the analysis. At all coverages, the O_d position distributions exhibit two most probable orientations, one maximized at $\varphi = 0°$ and the second extended from 40 to 90° and maximized at $\varphi \cong 65°$. The populations of the molecular orientation and the average height of O_d above the Ti_{5c} ions as a function of φ can be very clearly seen in the 2D plots shown in the middle and bottom panels, respectively. The former configuration has CO_2 essentially laying down flat ($\psi = 90°$) on the surface with O_d height of ∼1.3 Å below that of the CO_2 species at $\varphi = 45−90°$. Note that the distance of the flat lying CO_2 from the surface is approximately equal to that of the C atoms of the tilted CO_2 at $\varphi = 45−90°$, creating a T shaped dimer, which is a common feature in both liquid and solid CO_2 structures.[63,86] This configuration can be observed at all coverages in the AIMD snapshots in Figure 9A. Interestingly, the $\varphi = 0°$ configurations are not likely to be observed in the STM images, due to their low height but would be observed in IRAS spectra, thus reconciling the seemingly contradicting results. What is most remarkable is that the flat lying CO_2 configurations are observed with about 25% probability at 1/2−2/3 coverage with a decreasing population (ca. ∼10%) at 1 ML, which is exactly the inverse of what would be anticipated if CO_2-CO_2 interactions were the sole dominating factor controlling the structures of these films.

The second feature around $\varphi = 45−90°$ corresponds to the tilted CO_2 configuration with $\psi \cong 45°$. Rotation between the two minima is probable at all coverages with an estimated free energy barrier (obtained by taking the natural logarithm of $P(\varphi)$) of 0.06−0.07 eV at all coverages. The isotropic distribution of CO_2 orientations fits well with the ensemble-averaged CO_2 orientation from IRAS spectra (Figures 6 and 7), showing that CO_2 is tilted away from the surface normal and has components along both 0 and 90° azimuths. In contrast, the STM images obtained on

26331

dx.doi.org/10.1021/jp308061j | J. Phys. Chem. C 2012, 116, 26322−26334

oxidized $TiO_2(110)$ at low coverages ($\leq 1/2$ ML) are not in agreement with the AIMD results. Although the significant population of CO_2 at $\varphi = 0°$ azimuth would likely not be observable in the STM images, the bright spots in the STM images suggest tilt of CO_2 molecules along the $\varphi = 90°$ azimuth (Figures 2 and 4B(d)). The origin of this discrepancy is unclear.[87] Because the energy differences between different azimuthal configurations of isolated CO_2 molecules are small (<0.05 eV, Figure 3C) minor artifacts can alter the observed configurations both in the STM experiments and AIMD calculations. For example, non-negligible interactions of CO_2 with the STM tip (illustrated in section 3.2) may possibly lead to such effect. This conclusion would be aligned with the STM images obtained at 2/3 ML (Figure 4B(b,e)) where a position of the CO_2 related bright spots indicates tilt at $\varphi \cong 55 \pm 10°$ in accord with IRAS and the AIMD. Nonetheless, it is important to note that the relative free energy is about 0.01 eV; thus it is equally likely that an overestimation of CO_2–CO_2 contacts relative to CO_2–O_b contacts by DFT-D could also explain this discrepancy.

In addition to the features already discussed in the CO_2 distribution maps (Figure 10), the coverage of 1 ML exhibits an additional narrow band for $\varphi = 60–90°$ at longer Ti_{5c}–O_d distances (~2.3 Å). This feature arises from a non-negligible population (~9%) of CO_2 molecules that lie parallel to the surface on top of the O_b row. One such molecule can be observed in the AIMD snapshot shown in Figure 9. For the $T = 0$ K potential energy surface calculated at low coverage, this CO_2 species (Figure S1(h), Supporting Information) was found to be 0.24 eV less-tightly bound than the lowest energy Ti_{5c}-bound CO_2 species (Figure 3A(r1) and Figure S1(a), Supporting Information). At 1 ML, however, the binding energy of this site is found to be about 0.45–0.49 eV, depending on which molecule is chosen. This binding energy is significantly higher than that for the isolated CO_2 species bound at O_b sites and is in qualitative agreement with the binding energies for those bound at Ti_{5c} sites (as one would expect from the fact that they are in thermal equilibrium at this coverage). This observation would imply that CO_2–CO_2 intermolecular interactions are in part responsible for stabilizing this configuration. It is noted, however, that for 1.5 ML for which short AIMD simulations were performed (data not shown) the additional CO_2 molecules occupy O_b sites and have a binding energy of only 0.35 eV in agreement with the assignment of the 122 K peak in the TPD of Figure 5 which appears for coverages above 1 ML.

We now speculate on the origin of the disorder observed in our AIMD simulations. This dynamic change of configurations comes due to non-negligible interactions among CO_2 molecules comparing to that between CO_2 and the surface. To estimate the energetics of those two interactions, the pair distribution functions, $g(r)$, of C of CO_2 with O of another CO_2 (O_C) and O_b of the TiO_2 surface are considered. These distribution functions can be converted to potential of a mean force (PMF)[88] by $A(r) = -k_B T \ln(g(r))$ that allow us to quantify the magnitude of the interactions between these species (Figure S9, Supporting Information). The first nearest neighbor peaks are located at about 3.0 Å for both types of contacts regardless of the coverage, and this implies there is competitive interaction of a CO_2 with neighboring CO_2 and O_b on the surface. This is found to indeed be the case at 1 ML where the free energies of CO_2–CO_2 and CO_2–O_b are ~0.05 and ~0.06 eV, respectively. These interactions are about a factor of 8 smaller than the ca. 0.40 eV Ti_{5c}–O_a interactions inferred from binding energies but nonetheless non-negligible. Similar to the interactions of CO_2 molecules in the gas

phase,[64] typical CO_2 interactions can be classified as T-shaped quadrupole–quadrupole interaction or slipped parallel dipole–dipole interaction with interaction energies of 0.06 and 0.07 eV, respectively. When these interactions are compared to the CO_2 interaction with neighboring CO_2 and O_b on $TiO_2(110)$, they are quite similar in binding free energy and also in the interacting configuration.

Therefore, our results suggest that the presence of these two distinct types of weak interactions of CO_2 to neighboring CO_2 and O_b of TiO_2 surface create a corrugated potential energy landscape with relatively low barriers for CO_2 rotation and diffusion that leads to only a partial orientational ordering of the majority of CO_2 molecules which is consistent with our STM images. However, the CO_2 configurations such as lying flat on the surface or on O_b rows are not negligible due to high dynamical mobility of CO_2 molecules and would not be visible in STM but may be the origin of the more isotropically distributed C–O stretching modes seen in our IRAS studies.

4. SUMMARY

A combination of experimental investigations using scanning tunneling microscopy, infrared reflection adsorption spectroscopy, molecular beam techniques, and temperature programmed desorption with theoretical studies by dispersion-corrected density functional theory and ab initio molecular dynamics was used to attain detailed level of understanding about CO_2 adsorption, site specific binding, translational and rotational diffusion dynamics and desorption kinetics on rutile $TiO_2(110)$ surface. Given the breadth of this study we now integrate our observations to provide a comprehensible description of the coverage dependence of CO_2 behavior on rutile $TiO_2(110)$:

CO_2 Adsorption in Bridging Oxygen Vacancies (V_O's). The V_O defect sites are the most favorable adsorption sites and are populated first (STM). The theoretically (DFT+U) determined binding energy of 0.60 eV for CO_2 in a vacancy is in a fair agreement with the experimentally determined desorption energy of 0.45 ± 0.07 eV in the highest temperature (~160 K) TPD peak. In accord with prior literature, the V_O-bound CO_2 is observed to be easily reduced to CO and healed V_O using high bias (~ 3 V) STM scan.

On the basis of experiments using a flux calibrated molecular beam, the amount of CO_2 desorbing at 160 K is about three times the coverage of V_O sites. The two types of CO_2 associated with this 160 K TPD feature are confirmed by two sequentially populated vibrational frequencies at 2342.2 and 2346.5 cm^{-1} observed in IRAS. DFT+U calculations show that the V_O-bound CO_2 stabilizes the binding of additional CO_2 on neighboring Ti_{5c} sites, explaining the excess CO_2 observed in TPD.

CO_2 on Ti_{5c} Sites at Low Coverages. Isolated CO_2 molecules are observed to be highly mobile even at 50 K. The STM images acquired on V_O-free regions show tracks that represent a time average of all the positions visited by the rapidly diffusing CO_2. The tracks show two bright maxima separated by 2.6 Å and aligned along [1$\bar{1}$0] direction (across the O_b and Ti_{5c} rows) with the underlying Ti_{5c} sites. The DFT calculations on defect-free $TiO_2(110)$ show that isolated CO_2 binds through one of the O atoms on top of Ti_{5c} site and is tilted toward one of the neighboring O_b rows. The theoretically determined binding energy of CO_2 in this configuration is 0.45 eV in excellent agreement with the desorption energy of 0.38 ± 0.06 eV determined experimentally via TPD. Low barrier rotational motion allows for rapid switching of the tilted CO_2 between the two neighboring O_b rows. Rotation proceeds via configuration with flat-lying CO_2

bound with both O atoms to neighboring Ti_{5c} sites. This configuration is only slightly lower in energy providing for an extremely low rotational barrier. The same configuration is also responsible for very low diffusion barrier that proceeds via rotation and tumbling mechanism. The freely diffusing CO_2 is observed up to coverages of ~1/2 ML.

CO_2 on Ti_{5c} Sites at High Coverages. At 50 K, CO_2 diffusion is observed to cease at ~2/3 ML coverage. At this coverage, pairs of CO_2 molecules bound on neighboring Ti_{5c} sites are observed with a free Ti_{5c} site separating the pairs. The CO_2 molecules in the pairs are tilted away from each other and the free Ti_{5c} sites allow for unhindered rotation between the equivalent tilt positions. As the coverage increases to 1 ML, all Ti_{5c} sites become occupied and rotation motion also ceases leading to zigzag arrangement of tilted CO_2 molecules. IRAS results show that at all coverages CO_2 molecules are tilted away from cross row direction by ~45° which is in agreement with the AIMD calculations and consistent with STM images. The theoretical calculations show that the exact orientation of CO_2 molecules is a result of the fine balance between attractive quadrupole−quadrupole interactions and steric repulsion.

CO_2 on O_b Sites. TPD studies show that only 0.5 ML of CO_2 can bind on O_b rows with a desorption energy of 0.34 ± 0.05 eV. The limiting 0.5 ML coverage is found to be a result of an out-of-phase zigzag arrangement of CO_2 on neighboring Ti_{5c} rows that, while blocking half of the O_b sites, allows for 0.5 ML adsorption of strongly bound CO_2 on top of O_b's. The relatively high binding energy for CO_2 adsorbed on O_b sites (~ 0.4 eV) is found to be a result of strong quadrupole−quadrupole interactions with Ti_{5c} bound CO_2 molecules.

In conclusion, our detailed combined experimental and theoretical study provides insight into CO_2 binding configurations on surface sites on $TiO_2(110)$, demonstrates their highly dynamic nature and shows that quadrupole−quadrupole interactions play an important role in determining the detailed surface structures at different coverages.

ASSOCIATED CONTENT

Ⓢ Supporting Information
Calculated binding configurations of a single CO_2 molecule on $TiO_2(110)$; STM images illustrating the preparation of V_O free $TiO_2(110)$; STM image of diffusing CO_2; coverage-dependent CO_2 sticking coefficient, TPD spectra, and desorption energy; calculated CO_2 binding configurations on $TiO_2(110)$ with V_O's; distribution of O_a-O_a distances, O_d-O_d distances, pair distribution functions, and potentials of a mean force obtained from AIMD simulations. This material is available free of charge via the Internet at http://pubs.acs.org.

AUTHOR INFORMATION

Corresponding Author
*E-mail: N.G.P., Nikolai.Petrik@pnnl.gov; R.R., Roger. Rousseau@pnnl.gov; Z.D., Zdenek.Dohnalek@pnnl.gov.

Author Contributions
‡These authors contributed equally.

Notes
The authors declare no competing financial interest.

ACKNOWLEDGMENTS

REFERENCES

(1) Marini, L. *Geological Sequestration of Carbon Dioxide*; Elsevier: Amsterdam, 2006.
(2) *Handbook of Heterogeneous Catalysis*, 2nd ed.; Ertl, G.; Knözinger, H.; Schüth, F.; Weitkamp, J., Eds.; Wiley: Weinheim, 2008.
(3) Olah, G. A.; Goeppert, A.; Prakash, G. K. S. *Beyond Oil and Gas: The Methanol Economy*, 2nd ed.; Wiley: Weinheim, 2009.
(4) *Carbon Dioxide as Chemical Feedstock*; Aresta, M., Ed.; Wiley: Weinheim, 2010.
(5) Freund, H. J.; Roberts, M. W. *Surf. Sci. Rep.* **1996**, *25*, 225−273.
(6) Wang, J.; Burghaus, U. *J. Chem. Phys.* **2005**, *122*, 044705.
(7) Hotan, W.; Gopel, W.; Haul, R. *Surf. Sci.* **1979**, *83*, 162−180.
(8) Voigts, F.; Bebensee, F.; Dahle, S.; Volgmann, K.; Maus-Friedrichs, W. *Surf. Sci.* **2009**, *603*, 40−49.
(9) Kadossov, E.; Burghaus, U. *J. Phys. Chem. C* **2008**, *112*, 7390−7400.
(10) Henderson, M. A. *Surf. Sci.* **1998**, *400*, 203−219.
(11) Thompson, T. L.; Diwald, O.; Yates, J. T. *J. Phys. Chem. B* **2003**, *107*, 11700−11704.
(12) Suzanne, J.; Panella, V.; Ferry, D.; Sidoumou, M. *Surf. Sci.* **1993**, *293*, L912−L916.
(13) Seiferth, O.; Wolter, K.; Dillmann, B.; Klivenyi, G.; Freund, H. J.; Scarano, D.; Zecchina, A. *Surf. Sci.* **1999**, *421*, 176−190.
(14) Kuhlenbeck, H.; Xu, C.; Dillmann, B.; Hassel, M.; Adam, B.; Ehrlich, D.; Wohlrab, S.; Freund, H. J.; Ditzinger, U. A.; Neddermeyer, H.; et al. *Ber. Bunsen-Ges. Phys. Chem.* **1992**, *96*, 15−27.
(15) Wang, Y.; Lafosse, A.; Jacobi, K. *J. Phys. Chem. B* **2002**, *106*, 5476−5482.
(16) Wang, H. Y.; Schneider, W. F. *Phys. Chem. Chem. Phys.* **2010**, *12*, 6367−6374.
(17) Hinojosa, J. A.; Antony, A.; Hakanoglu, C.; Asthagiri, A.; Weaver, J. F. *J. Phys. Chem. C* **2012**, *116*, 3007−3016.
(18) Onishi, H.; Iwasawa, Y. *Catal. Lett.* **1996**, *38*, 89−94.
(19) Lavalley, J. C. *Catal. Today* **1996**, *27*, 377−401.
(20) Funk, S.; Hokkanen, B.; Johnson, E.; Burghaus, U. *Chem. Phys. Lett.* **2006**, *422*, 461−465.
(21) Indrakanti, V. P.; Kubicki, J. D.; Schobert, H. H. *Energ. Fuel* **2008**, *22*, 2611−2618.
(22) Takahashi, H.; Yuki, K.; Nitta, T. *Fluid Phase Equilib.* **2002**, *194*, 153−160.
(23) Anpo, M.; Yamashita, H.; Ichihashi, Y.; Ehara, S. *J. Electroanal. Chem.* **1995**, *396*, 21−26.
(24) Lee, J.; Sorescu, D. C.; Deng, X.; Jordan, K. D. *J. Phys. Chem. Lett.* **2011**, *2*, 3114−3117.
(25) Lee, J.; Sorescu, D. C.; Deng, X. Y. *J. Am. Chem. Soc.* **2011**, *133*, 10066−10069.
(26) Ramis, G.; Busca, G.; Lorenzelli, V. *Mater. Chem. Phys.* **1991**, *29*, 425−435.
(27) Busca, G.; Lorenzelli, V. *Mater. Chem.* **1982**, *7*, 89−126.
(28) Funk, S.; Burghaus, U. *Phys. Chem. Chem. Phys.* **2006**, *8*, 4805−4813.
(29) Gopel, W.; Rocker, G.; Feierabend, R. *Phys. Rev. B* **1983**, *28*, 3427−3438.
(30) Cybula, A.; Klein, M.; Zielinska-Jurek, A.; Janczarek, M.; Zaleska, A. *Physicochem. Probl. Miner. Process.* **2012**, *48*, 159−167.
(31) Gutierrez-Sosa, A.; Walsh, J. F.; Lindsay, R.; Wincott, P. L.; Thornton, G. *Surf. Sci.* **1999**, *433*, 538−542.
(32) Krischok, S.; Hofft, O.; Kempter, V. *Surf. Sci.* **2002**, *507*, 69−73.

(33) Markovits, A.; Fahmi, A.; Minot, C. *J. Mol. Struct. (THEOCHEM)* **1996**, *371*, 219−235.

(34) Tan, S. J.; Zhao, Y.; Zhao, J.; Wang, Z.; Ma, C. X.; Zhao, A. D.; Wang, B.; Luo, Y.; Yang, J. L.; Hou, J. G. *Phys. Rev. B* **2011**, *84*, 155418.

(35) Sorescu, D. C.; Lee, J.; Al-Saidi, W. A.; Jordan, K. D. *J. Chem. Phys.* **2011**, *134*, 104707.

(36) Sorescu, D. C.; Al-Saidi, W. A.; Jordan, K. D. *J. Chem. Phys.* **2011**, *135*, 124701.

(37) Indrakanti, V. P.; Schobert, H. H.; Kubicki, J. D. *Energ. Fuel.* **2009**, *23*, 5247−5256.

(38) Indrakanti, V. P.; Kubicki, J. D.; Schobert, H. H. *Fuel Process. Technol.* **2011**, *92*, 805−811.

(39) Indrakanti, V. P.; Kubicki, J. D.; Schobert, H. H. *Energ. Environ. Sci.* **2009**, *2*, 745−758.

(40) Civis, S.; Ferus, M.; Kubat, P.; Zukalova, M.; Kavan, L. *J. Phys. Chem. C* **2011**, *115*, 11156−11162.

(41) Acharya, D. P.; Camillone, N.; Sutter, P. *J. Phys. Chem. C* **2011**, *115*, 12095−12105.

(42) Salem, I. *Catal. Rev.* **2003**, *45*, 205−296.

(43) Inoue, T.; Fujishima, A.; Konishi, S.; Honda, K. *Nature* **1979**, *277*, 637−638.

(44) Pang, C. L.; Lindsay, R.; Thornton, G. *Chem. Soc. Rev.* **2008**, *37*, 2328−2353.

(45) Roy, S. C.; Varghese, O. K.; Paulose, M.; Grimes, C. A. *Acs Nano* **2010**, *4*, 1259−1278.

(46) Zhang, Z.; Bondarchuk, O.; Kay, B. D.; White, J. M.; Dohnalek, Z. *J. Phys. Chem. B* **2006**, *110*, 21840−21845.

(47) Feibelman, P. J.; Kimmel, G. A.; Smith, R. S.; Petrik, N. G.; Zubkov, T.; Kay, B. D. *J. Chem. Phys.* **2011**, *134*, 204702.

(48) Dohnalek, Z.; Kim, J.; Bondarchuk, O.; White, J. M.; Kay, B. D. *J. Phys. Chem. B* **2006**, *110*, 6229−6235.

(49) Horcas, I.; Fernandez, R.; Gomez-Rodriguez, J. M.; Colchero, J.; Gomez-Herrero, J.; Baro, A. M. *Rev. Sci. Instrum.* **2007**, *78*, 013705.

(50) Henderson, M. A. *Surf. Sci. Rep.* **2002**, *46*, 1−308.

(51) Diebold, U. *Surf. Sci. Rep.* **2003**, *48*, 53−229.

(52) Zhang, Z. R.; Bondarchuk, E.; Kay, B. D.; White, J. M.; Dohnalek, Z. *J. Phys. Chem. C* **2007**, *111*, 3021−3027.

(53) Henderson, M. A. *Langmuir* **1996**, *12*, 5093−5098.

(54) The CP2K developers group. http://cp2k.org/, (2009).

(55) VandeVondele, J.; Krack, M.; Mohamed, F.; Parrinello, M.; Chassaing, T.; Hutter, J. *Comput. Phys. Commun.* **2005**, *167*, 103−128.

(56) Lippert, G.; Hutter, J.; Parrinello, M. *Mol. Phys.* **1997**, *92*, 477−487.

(57) Perdew, J. P.; Burke, K.; Ernzerhof, M. *Phys. Rev. Lett.* **1996**, *77*, 3865−3868.

(58) Goedecker, S.; Teter, M.; Hutter, J. *Phys. Rev. B* **1996**, *54*, 1703−1710.

(59) VandeVondele, J.; Hutter, J. *J. Chem. Phys.* **2007**, *127*, 114105.

(60) Grimme, S. *J. Comput. Chem.* **2006**, *27*, 1787−1799.

(61) Zhang, Z. R.; Rousseau, R.; Gong, J. L.; Kay, B. D.; Dohnalek, Z. *J. Am. Chem. Soc.* **2009**, *131*, 17926−17932.

(62) Kwak, J. H.; Rousseau, R.; Mei, D. H.; Peden, C. H. F.; Szanyi, J. *ChemCatChem* **2011**, *3*, 1557−1561.

(63) Glezakou, V. A.; Rousseau, R.; Dang, L. X.; McGrail, B. P. *Phys. Chem. Chem. Phys.* **2010**, *12*, 8759−8771.

(64) Windisch, C. F.; Glezakou, V. A.; Martin, P. F.; McGrail, B. P.; Schaef, H. T. *Phys. Chem. Chem. Phys.* **2012**, *14*, 2560−2566.

(65) Mills, G.; Jonsson, H.; Schenter, G. K. *Surf. Sci.* **1995**, *324*, 305−337.

(66) Henkelman, G.; B.P., U.; Jonsson, H. *J. Chem. Phys.* **2000**, *113*, 9901−9904.

(67) Nose, S. *J. Chem. Phys.* **1984**, *81*, 511−519.

(68) Hoover, W. G. *Phys. Rev. A* **1985**, *31*, 1695−1697.

(69) Dudarev, S. L.; Botton, G. A.; Savrasov, S. Y.; Humphreys, C. J.; Sutton, A. P. *Phys. Rev. B* **1998**, *57*, 1505−1509.

(70) Borodin, A.; Reichling, M. *Phys. Chem. Chem. Phys.* **2011**, *13*, 15442−15447.

(71) Yim, C. M.; Pang, C. L.; Thornton, G. *Phys. Rev. Lett.* **2010**, *104*, 036806.

(72) Rittner, F.; Boddenberg, B.; Bojan, M. J.; Steele, W. A. *Langmuir* **1999**, *15*, 1456−1462.

(73) Kunat, M.; Traeger, F.; Silber, D.; Qiu, H.; Wang, Y.; van Veen, A. C.; Woll, C.; Kowalski, P. M.; Meyer, B.; Hattig, C.; et al. *J. Chem. Phys.* **2009**, *130*, 144703.

(74) King, D. A.; Wells, M. G. *Surf. Sci.* **1972**, *29*, 454−482.

(75) Dohnalek, Z.; Kimmel, G. A.; Joyce, S. A.; Ayotte, P.; Smith, R. S.; Kay, B. D. *J. Phys. Chem. B* **2001**, *105*, 3747−3751.

(76) Li, Z. J.; Smith, R. S.; Kay, B. D.; Dohnalek, Z. *J. Phys. Chem. C* **2011**, *115*, 22534−22539.

(77) Tait, S. L.; Dohnalek, Z.; Campbell, C. T.; Kay, B. D. *J. Chem. Phys.* **2005**, *122*, 164707.

(78) Schaich, W. L.; Chen, W. *Phys. Rev. B* **1989**, *39*, 10714−10724.

(79) Chabal, Y. J. *Surf. Sci. Rep.* **1988**, *8*, 211−357.

(80) Hansen, W. N. *Symp. Faraday Soc.* **1970**, *4*, 27−35.

(81) Richter, L. J.; Buntin, S. A.; Chu, P. M.; Cavanagh, R. R. *J. Chem. Phys.* **1994**, *100*, 3187−3200.

(82) Chen, W.; Schaich, W. L. *Surf. Sci.* **1989**, *220*, L733−L739.

(83) Deskins, N. A.; Rousseau, R.; Dupuis, M. *J. Phys. Chem. C* **2011**, *115*, 7562−7572.

(84) Saharay, M.; Balasubramanian, S. *J. Chem. Phys.* **2004**, *120*, 9694−9702.

(85) Saharay, M.; Balasubramanian, S. *J. Phys. Chem. B* **2007**, *111*, 387−392.

(86) Santoro, M.; Gorelli, F. A. *Chem. Soc. Rev.* **2006**, *35*, 918−931.

(87) On the other hand, the ensemble-averaged IRAS spectra in Figures 6 and 7 do not provide information on relative contribution of various individual molecular orientations. For example, if the spectra are combined predominantly from 2 orientations, flat at $\varphi = 0°$ and $\psi = 90°$ and tilted with $\varphi = 90°$ and $\psi = 45°$, the molecule should spend twice more time in the latter configuration to satisfy results in Figure 6A,B. This example is more consistent with the STM data for low coverages.

(88) McQuarrie, D. A. *Statistical Mechanics*; University Science Books: Sausalito, CA, 2000.